Influence of traps reversibility on hydrogen permeation and retention in Eurofer97

F. Montupet-Leblond, E.A. Hodille, M. Payet, R. Delaporte-Mathurin, E. Bernard, Y. Charles, J. Mougenot, S. Vartanian, C. Grisolia

Influence of traps reversibility on hydrogen permeation and retention in Eurofer97

F. Montupet-Leblond[a,*], E. A. Hodille[a], M. Payet[a], R. Delaporte-Mathurin[a,b], E. Bernard[a], Y. Charles[b], J. Mougenot[b], S. Vartanian[a], C. Grisolia[a]

[a] *Institut de Recherche sur la Fusion par Confinement Magnétique, CEA Cadarache, 13115 St Paul lez Durance, France*
[b] *Université Sorbonne Paris Nord, Laboratoire des Sciences des Procédés et des Matériaux, LSPM, CNRS, UPR 3407, F-93430, Villetaneuse, France*

Abstract

The presence of three trapping sites in Eurofer97 and the diffusion and trapping parameters obtained in a previous article are confirmed using an additional thermal desorption spectrometry (TDS) experiment. Using these parameters, permeation cycles are simulated using the diffusion-reaction code MHIMS in order to study the influence of each trapping site on the permeation dynamics. The concept of traps reversibility is used to qualify this influence. The analysis indicates that the reversibility of the trapping sites is a key parameter in diffusion and permeation dynamics, which must be accounted for to get accurate predictions of hydrogen inventory and permeation.

Keywords: Hydrogen permeation, Trap reversibility, Eurofer97, Diffusion-trapping, TDS, MHIMS, modelling

1. Introduction

During the operation of fusion reactors, the plasma-facing components (PFCs) are exposed to high particles fluxes, including tritium. The use of this element in the D-T reaction leads to a number of challenges [**?**] such as tritium economy and accountancy. In particular for ITER, safety regulations set the maximum in-vessel retention to 700 g [**?**] and call for a careful prediction of the retention and of the amount of tritium permeating up to the coolant. These evaluations can be performed using diffusion-trapping codes [**? ? ? ? ? ? ? ? ? ?**] that rely on material properties such as diffusivity, solubility and trapping densities and energies.

In the case of DEMO, Eurofer97 is foreseen as a structural material [**? ?**]. The diffusion and trapping characteristics of this material were investigated in [**?**]. The permeation results revealed that trapping had an influence on diffusivity and solubility, and were consequently fitted using the effective diffusivity and solubility in order to take this trapping behavior into account. In particular, this model indicated the presence of a low detrapping energy trapping site (0.5 eV). The transport parameters values where shown to be in agreement with the observations of several authors [**? ? ?**]. However, the thermal desorption spectrometry (TDS) experiment performed up to 800 K identified a total of three trapping sites, two of which correspond to higher detrapping energies, in agreement with [**?**].

The present work aims at investigating the presence of these high detrapping energy trapping sites and their impact on the results of permeation experiments performed between 473 K and 723 K. In the first part of this article, the presence of these high detrapping energy trapping sites is confirmed with an additional TDS experiment performed up to 1273 K, coupled to a simulation performed with the reaction-diffusion code MHIMS.

In the second part, the influence of each trapping site on the permeation dynamics is investigated with simulations of permeation experiments performed with MHIMS. In accordance with previous observations [**? ? ? ? ? ?**], irreversible trapping sites are shown to have an impact on permeation. A definition of reversibility is given in [**?**]: "a reversible trap is one at which hydrogen has a short residence time at the temperature of interest with an equivalent low detrapping energy. On the other hand, for the same conditions, an irreversible trap is one with a negligible probability of releasing its hydrogen". Reversibility is commonly used in the field of hydrogen embrittlement studies, that take place at room temperature; however, reversibility has been shown to be linked to temperature in [**? ?**]. In order to extend this notion to fusion materials operating at higher temperatures, the present work investigates trap reversibility as a function of temperature. This analysis shows in particular that the high-energy trapping site in Eurofer97 is irreversible in the entire operational temperature range of Eurofer97 [**?**], which impacts the kinetics of permeation in the case of cyclic loading as already observed in iron and steels [**? ? ? ?**].

Lastly, the permeation timelag and tritium inventory are

*Corresponding author
Email address: floriane.leblond@cea.fr
(F. Montupet-Leblond)

evaluated with the MHIMS code (which is a detailed code taking into account diffusion, trapping and surface effects) and with the simplified effective diffusivity model. The comparison between these results indicates that the assumptions that are necessary to obtain the effective diffusivity model do not cover irreversibility effects. Therefore, this model overlooks part of the trapping behavior of hydrogen isotopes in Eurofer97, leading to a possible under-evaluation of retention.

2. Modelling

2.1. Diffusion-trapping model

The model of hydrogen isotopes migration used in MHIMS is derived from the McNabb & Foster equations [**? ?**]. In this model, hydrogen particles in the bulk are considered as either mobile or trapped. The evolution of mobile (C_m, m^{-3}) and trapped ($C_{\mathrm{t},i}$, m^{-3}) particles in the bulk is given by equations (1)-(2):

$$\frac{\partial C_{\mathrm{t},i}}{\partial t} = p \cdot C_\mathrm{m}\big(N_{\mathrm{t},i} - C_{\mathrm{t},i}\big) - k_i \cdot C_{\mathrm{t},i} \tag{1}$$

$$\frac{\partial C_\mathrm{m}}{\partial t} = D(T)\frac{\partial^2 C_\mathrm{m}}{\partial x^2} - \sum \frac{\partial C_{\mathrm{t},i}}{\partial t} \tag{2}$$

In equation (2), D is the diffusivity, expressed as

$$D(T) = D_0 \cdot \exp\Big(-\frac{E_D}{k_B T}\Big) \tag{3}$$

where D_0 ($\mathrm{m}^2.\mathrm{s}^{-1}$) is the pre-exponential diffusivity coefficient and E_D (eV) is the diffusion energy.

The trapping and detrapping parameters p ($\mathrm{m}^{-3}.\mathrm{s}^{-1}$) and k_i (s^{-1}) are taken as

$$p(T) = \frac{\nu_0}{N_\mathrm{L}} \exp\Big(-\frac{E_\mathrm{D}}{k_B T}\Big) \tag{4}$$

$$k_i(T) = \nu_0 \exp\Big(-\frac{E_{\mathrm{dt},i}}{k_B T}\Big) \tag{5}$$

where ν_0 (s^{-1}) is the pre-exponential frequency for trapping and detrapping, $E_{\mathrm{dt},i}$ (eV) is the detrapping energy for trapping site i and $N_{\mathrm{t},i}$ (m^{-3}) is the associated density. The detrapping energy is usually taken as the sum of binding energy E_b and diffusion energy E_D.

This model relies on two assumptions regarding the lattice density N_L (m^{-3}), which models the number of possible interstitial sites:

- $N_\mathrm{L} \gg \sum_i N_{\mathrm{t},i}$: each trapping site is surrounded by lattice sites only, and re-trapping cannot happen directly upon detrapping;
- $N_\mathrm{L} \gg C_\mathrm{m}$: there are enough free lattice sites for any trapped Q atom to detrap into an interstitial site.

2.2. Effective diffusivity derivation

Diffusivity as presented in equation (3) only involves interstitial processes. This definition can be extended in order to take into account the contribution of trapping effects, which are expected to slow down the diffusion of particles through a given material, especially at lower temperatures.

In the following, trapping is modeled by a single trap described by its density N_t (m^{-3}), its binding energy E_b (eV). The concentration associated to this trapping site is C_t (m^{-3}).

Using

$$\frac{\partial C_{\mathrm{t},i}}{\partial t} = \frac{\partial C_{\mathrm{t},i}}{\partial C_\mathrm{m}} \cdot \frac{\partial C_\mathrm{m}}{\partial t} \tag{6}$$

equation (2) can be rewritten as

$$\begin{aligned} \frac{\partial C_\mathrm{m}}{\partial t} &= D(T)\frac{\partial^2 C_\mathrm{m}}{\partial x^2} - \frac{\partial C_\mathrm{m}}{\partial t}\frac{\partial C_\mathrm{t}}{\partial C_\mathrm{m}} \\ \Leftrightarrow \Big(1 + \frac{\partial C_\mathrm{t}}{\partial C_\mathrm{m}}\Big)\frac{\partial C_\mathrm{m}}{\partial t} &= D(T)\frac{\partial^2 C_\mathrm{m}}{\partial x^2} \\ \Leftrightarrow \frac{\partial C_\mathrm{m}}{\partial t} &= \frac{D(T)}{1 + \dfrac{\partial C_\mathrm{t}}{\partial C_\mathrm{m}}}\frac{\partial^2 C_\mathrm{m}}{\partial x^2} \end{aligned} \tag{7}$$

Equation (7) is equivalent to Fick's second law of diffusion with a modified diffusion coefficient that will be called effective diffusivity from now on [**?**]:

$$D_\mathrm{eff} = \frac{D(T)}{1 + \dfrac{\partial C_\mathrm{t}}{\partial C_\mathrm{m}}} \tag{8}$$

The $\frac{\partial C_\mathrm{t}}{\partial C_\mathrm{m}}$ quantity is linked to the equilibrium between interstitial and trapped Q atoms:

$$\mathrm{Trap}_\mathrm{empty} + \mathrm{Q}_\mathrm{mobile} \leftrightarrow \mathrm{Q}_\mathrm{trapped} + \mathrm{Lattice\ site}_\mathrm{empty} \tag{9}$$

The corresponding reaction constant depends on the difference between the energy level of mobile and trapped particles, which is E_b:

$$K_\mathrm{trap} = \exp\Big(\frac{E_b}{k_B T}\Big) \tag{10}$$

This reaction constant can also be expressed as a function of the densities and concentrations:

$$K_\mathrm{trap} = \frac{C_\mathrm{t}\big(N_\mathrm{L} - C_\mathrm{m}\big)}{\big(N_\mathrm{t} - C_\mathrm{t}\big)C_\mathrm{m}} \tag{11}$$

$$= \frac{\theta_\mathrm{t}\big(1 - \theta_\mathrm{m}\big)}{\big(1 - \theta_\mathrm{t}\big)\theta_\mathrm{m}} \tag{12}$$

where $\theta_x = \dfrac{C_x}{N_x}$ is the occupancy of site x.

Following the assumption made in section 2.1 that $C_\mathrm{m} \ll N_L$, the occupancy of interstitial sites θ_m is low and the reaction constant can be simplified:

$$K_\mathrm{trap} = \frac{1}{\theta_m}\frac{\theta_\mathrm{t}}{1-\theta_t} \tag{13}$$

The quantity $\dfrac{\partial C_\mathrm{t}}{\partial C_\mathrm{m}}$ can be expressed using the occupancies if N_t is time-independent [**?**]:

$$\frac{\partial C_\mathrm{t}}{\partial C_\mathrm{m}} = \frac{N_\mathrm{t}}{N_\mathrm{L}}\frac{\partial \theta_\mathrm{t}}{\partial \theta_\mathrm{L}} \tag{14}$$

The derivative $\dfrac{\mathrm{d}\theta_\mathrm{t}}{\mathrm{d}\theta_\mathrm{m}}$ can be evaluated using the definition K_trap given in equation (13), as shown in [**?**]:

$$\frac{\mathrm{d}\theta_\mathrm{t}}{\mathrm{d}\theta_\mathrm{m}} = \frac{\mathrm{d}}{\mathrm{d}\theta_\mathrm{m}}\left(\frac{K_\mathrm{trap}\theta_\mathrm{m}}{1+K_\mathrm{trap}\theta_\mathrm{m}}\right) \tag{15}$$

$$= \frac{K_\mathrm{trap}}{\left(1+K_\mathrm{trap}\theta_\mathrm{m}\right)^2} \tag{16}$$

$$= K_\mathrm{trap}\left(1-\theta_t\right)^2 \tag{17}$$

Therefore,

$$\frac{\partial C_\mathrm{t}}{\partial C_\mathrm{m}} = \frac{N_\mathrm{t}}{N_\mathrm{L}}K_\mathrm{trap}\left(1-\theta_t\right)^2 \tag{18}$$

Combining equations (8) and (18), we can express effective diffusivity as

$$D_\mathrm{eff} = \frac{D}{1+\dfrac{N_\mathrm{t}}{N_\mathrm{L}}K_\mathrm{trap}\left(1-\theta_\mathrm{t}\right)^2} \tag{19}$$

If we consider the trap occupancy to be low, $\theta_\mathrm{t} \ll 1$ and equation (19) can be put under its final form:

$$D_\mathrm{eff} = \frac{D}{1+\dfrac{N_\mathrm{t}}{N_\mathrm{L}}\exp\left(\dfrac{E_b}{k_B T}\right)} \tag{20}$$

Equation (20) is commonly known as Oriani's equation for effective diffusivity [**?**]. This simple model includes a simplified trapping behavior in the usual diffusivity coefficient through the addition of two parameters relative to the trapping, namely the binding energy E_b and the associated density N_t. This interpolation is commonly used on experimental data when diffusivity shows signs of trapping-influenced behaviour [**?** **?** **?**].

However, the validity of equation (20) is limited due to the assumptions made on the material, which are:

- Trapping can be modeled by a single trap
- Trapped and interstitial hydrogen are at equilibrium (Oriani's assumption)
- Interstitial occupancy is low
- Trap occupancy is low

Therefore, this model is very different from the McNabb & Foster model that MHIMS relies on, which was introduced in 2.1. These differences are investigated in detail in section 5.

3. Identification of the three trapping sites

In this part, the transport and trapping parameters obtained in [**?**] are recalled, along with the corresponding experimental techniques. An additional TDS is presented to confirm the presence of a trapping site with high detrapping energy.

3.1. Gas-driven permeation experiments

The transport parameters of hydrogen isotopes in Eurofer97 have been determined in [**?**] with gas-driven permeation experiments performed using Hypertomate (HYdrogen PERmeation in TOkamak-relevant MATErials), a diagram of which is given in figure 1. In this setup, two high-vacuum enclosures are separated by a sample (thickness between 500 µm and 1 mm). During a run of the experiment, hydrogen is introduced stepwise in one of the chambers (upstream part). In isolated mode (valve V_2 is closed), the subsequent permeation flux induces a pressure rise on the downstream part, which contains information about the permeation dynamics in the material under scrutiny. On both

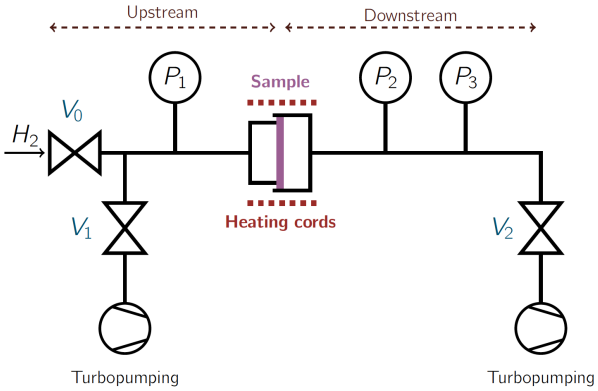

Figure 1: Diagram presenting the Hypertomate hydrogen permeation experiment

sides, the pressure is recorded using MKS® Baratron gauges (1000 Torr full gauge on the upstream side, 0.1 Torr full scale downstream). Hydrogen permeation experiments performed on Eurofer97 samples yield transport parameters such as effective diffusivity D_eff, effective solubility K_eff and permeability Φ. In particular for Eurofer97, D_eff contains partial information about

the trapping sites and shows that traps have an influence on permeation in the 473 K - 673 K range [?]. In the following, Hypertomate transport parameters presented in table 1 are used.

3.2. TDS experiments and MHIMS *analysis*

TDS experiments are performed on deuterium-loaded Eurofer97 samples using the device initially presented in [?] and used in [?]. This device named TEDDI (ThErmal Desorption of Deuterium in materIals) consists of a high vacuum enclosure equipped with a Bayard-Alpert pressure gauge and a quadrupole mass spectrometer. During the course of an experiment, a sample containing deuterium is heated up with a filament following a pre-defined ramp-up, controlled by a thermocouple inserted in the sample. The resulting desorption rate is recorded by the mass spectrometer, which is calibrated using the pressure gauge.

The sample is loaded beforehand by heating it up to 673 K in $9{\cdot}10^4$ Pa of deuterium, then quenched in order to prevent desorption from the trapping sites. This experimental procedure results in a TDS spectrum where peaks indicate the presence of several trapping sites.

In order to analyze this spectrum in detail, the full experiment (loading, thermal quenching, resting, temperature ramp-up) is simulated with MHIMS, using the transport parameters obtained with Hypertomate and recalled in table 1, as well as the surface model introduced in [? ?]. In the case of Eurofer97, this analysis yields the energies and densities of three trapping sites. These parameters values (resp. $E_{dt,i}$ and $N_{t,i}$ for trapping site i), as well as the energy barriers corresponding to the kinetic surface model used, are given in table 2. The TDS spectrum on which the analysis presented in [?] is based is presented in figure 2 as "First TDS up to 873 K". For this first experiment, the temperature is capped at 873 K in order to remain within the material specifications [?]. Above this temperature limit, even short-term heat exposure can result in overtempering of the martensite structure and softening of the metal. Noticeably, the desorption rate is not zero at 873 K, which means that deuterium remains in the sample at the end of the experiment. As shown with the MHIMS analysis, this interrupted peak indicates the presence of a trapping site with a high detrapping energy (referred to as trapping site number 3), which detrapping energy is $E_{dt,3} = 1.65$ eV.

In order to confirm the presence of the third trapping site and get a fuller understanding of trapping in Eurofer97, the TDS experiment presented in [?] is performed once again on the same sample, with the same temperature ramp-up (1 K/s) and the maximum temperature raised to 1273 K (TEDDI experimental limit), without breaking the vacuum. In-between the two temperature ramp-ups, the sample is left to cool down in the vacuum enclosure where the background pressure is $P_{bg} \sim 1 \cdot 10^{-6}$ Pa (i.e. the sample is not re-loaded in deuterium between the experiments). The corresponding experimental spectrum is shown in figure 2 and referred to as "Second TDS up to 1273 K". During the second TDS experiment, desorption takes over when the temperature reaches 873 K, following closely the interrupted peak visible in the first TDS. The peaks centered on 520 K and 1000 K reach equivalent maximum desorption values, meaning that the trapping sites desorbing in the 300 K - 873 K and in the 873 K - 1273 K ranges contain similar amounts of deuterium under these loading conditions. The second TDS spectrum also shows a shouldering around 1100 K, even though the temperature ramp-up remained stable in this region. Around this temperature, important metallurgical changes occur [?]: this additional flux could be explained by a release of internal stresses, a solubility modification, or the dissolution of inclusions, which would all have an impact on hydrogen transport. The investigation of the precise phenomena explaining this behavior is beyond the scope of the present analysis.

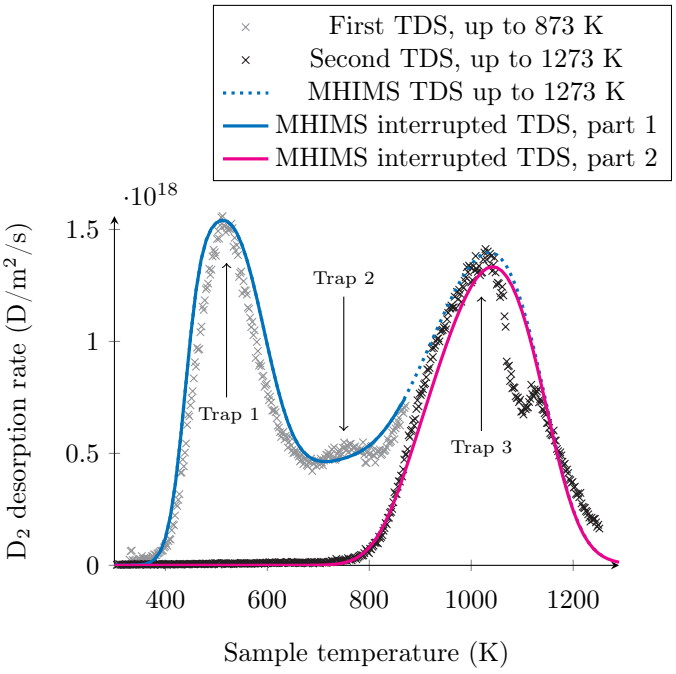

Figure 2: Interrupted TDS performed on deuterium-loaded Eurofer97, up to 873 k and then up to 1273 K. MHIMS simulations corresponding to the interrupted TDS and to a single TDS up to 1273 K are also shown.

In order to check the validity of the set of parameters obtained with the parametric optimization presented in [?], this interrupted TDS experiment is simulated using MHIMS. The boundary conditions rely on the kinetic surface model taken from [? ?]. Symmetry is rendered by a Neumann boundary condition with the normal hydrogen flux set to zero. The modeling steps, which replicate the experimental ones, are the following:

	D_0 ($m^2.s^{-1}$)	E_D (eV)	Φ_0 ($mol.m^{-1}.Pa^{-1/2}.s^{-1}$)	E_Φ (eV)	K_0 ($mol.m^{-3}.Pa^{-1/2}$)	E_K (eV)	N_t (m^{-3})	E_b (eV)
Hypertomate [**?**]	$2.52{\cdot}10^{-7}$	0.16	$4.43{\cdot}10^{-8}$	0.43	$1.76{\cdot}10^{-1}$	0.27	$6.08{\cdot}10^{25}$	0.42
Esteban [**?**]	$4.57{\cdot}10^{-7}$	0.23	$1.03{\cdot}10^{-8}$	0.39	$2.25{\cdot}10^{-2}$	0.16	$1.30{\cdot}10^{25}$	0.45
Aiello [**?**]	$1.50{\cdot}10^{-7}$	0.15	$1.53{\cdot}10^{-8}$	0.40	$1.02{\cdot}10^{-3}$	0.25	$1.04{\cdot}10^{24}$	0.60
Chen [**?**]	$3.15{\cdot}10^{-8}$	0.06	$1.26{\cdot}10^{-8}$	0.36	$4.00{\cdot}10^{-1}$	0.30	$4.50{\cdot}10^{23}$	0.78

Table 1: Arrhenius permeation parameters for hydrogen isotopes in Eurofer97

Name	Symbol	Value	Unit
Detrapping energies	$E_{dt,1}$	0.51	eV
	$E_{dt,2}$	1.27	
	$E_{dt,3}$	1.65	
Traps densities	$N_{t,1}$	$6.01 \cdot 10^{25}$	m^{-3}
	$N_{t,2}$	$6.44 \cdot 10^{22}$	
	$N_{t,3}$	$3.88 \cdot 10^{23}$	
Surface energies	E_A	1.32	eV
	E_R	0.65	
	$2E_{des}$	0.80	

Table 2: Detrapping energies, traps densities and surface energies E_A, E_R and E_{des} resulting from the TDS fit with MHIMS and a kinetic surface model. In the following, the traps will be referred to using their number, i.e. trap 1 for the 0.51 eV site, trap 2 for the 1.27 eV site and trap 3 for the 1.65 eV site.

1. Gas loading: constant temperature of 673 K and deuterium loading pressure of $9{\cdot}10^4$ Pa until sample saturation is reached.
2. Thermal quenching: temperature is lowered to 300 K abruptly (1 s). Consequently, deuterium pressure decreases to $4{\cdot}10^4$ Pa (sample quenching).
3. Resting/Pumping down: temperature remains at 300 K and deuterium pressure drops to 0 Pa. This condition models the very high vacuum conditions of the vacuum enclosure. This step corresponds to the insertion of the sample in the vacuum enclosure.
4. First TDS phase: deuterium pressure is 0 Pa on both sides, corresponding to the vacuum atmosphere of the device. Temperature is increased by 1 K/s, starting at 300 K and stopping at 873 K.
5. Cooling down: the temperature drops to 300 K abruptly (1 s).
6. Second TDS phase: temperature is increased by 1 K/s, starting at 300 K and stopping at 1273 K.

A single TDS with a maximum temperature of 1273 K (i.e. skipping steps 4 and 5) is also simulated. The corresponding simulated TDS spectrum is presented under "MHIMS TDS up to 1273 K" in figure 2. In the simulations, under the loading conditions of this TDS experiment, the quantities of particles desorbing from trapping sites 1 and 3 are close: this can be seen qualitatively on the TDS spectra, where peaks at 500 K and 1000 K have similar intensities and integral values.

The results of these simulations indicate that the parameters presented in table 2, which were inferred using only the TDS up to 873 K, describe accurately the full TDS.

4. Evaluation of the influence of trapping on permeation through cyclic simulations

In this section, the influence of trapping sites (reversible and irreversible) on permeation is investigated. MHIMS is used to simulate permeation experiments, after which the routine that is described in [**?**] and used on Hypertomate experimental data to extract D_{eff} is applied to simulated permeation results. The corresponding simulated effective diffusivity is compared to the experimental effective diffusivity in order to assess the validity of the three-traps model.

4.1. Simulations setup

Permeation simulations consist of a succession of loading and resting steps, of which an example is given in figure 3.

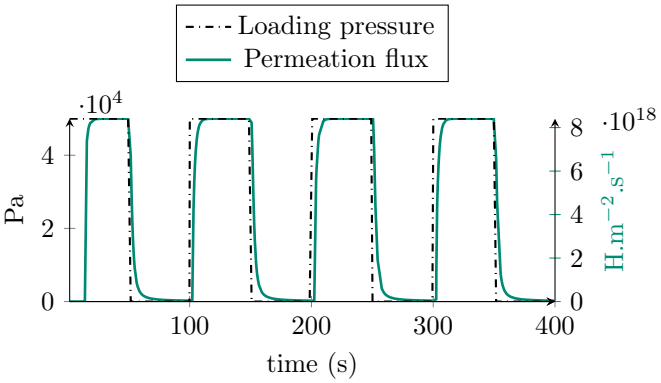

Figure 3: Example of a permeation simulation with a three-trap model at 673 K, showing four permeation cycles. Each cycle consists in a 50 s loading phase followed by a 50 s resting phase. Loading phases are considered complete when the permeation flux reaches its steady-state value.

A permeation cycle consists of the following steps:

1. Loading: the sample is exposed to $P_{loading} = 5 \cdot 10^4$ Pa of hydrogen at a fixed temperature. The duration of this step is chosen to be long enough for the permeation flux to reach a steady-state, as visible in figure 3.
2. Resting: the pressure drops down to 0 Pa and the permeation flux goes back to a constant value that is negligible as compared to the steady-state loading flux.

Loading and resting times are chosen in order to agree with the permeation experiments. Both surfaces are simulated using the kinetic surface model presented in [? ?] and used in the TDS simulations.

The first step of the analysis is to check that the permeation regime is diffusion-limited. The permeation flux is then integrated in order to obtain the pressure rise corresponding to hydrogen permeation taking place in a closed system. This pressure rise is processed using the steps presented in [?] (which are only valid for diffusion-limited permeation) in order to obtain the timelag τ_l (s). The simulations are performed between 473 K and 873 K: below 473 K and with the kinetic surface model, the permeation regime is not diffusion-limited and the analysis presented here cannot be performed.

Finally, the effective diffusivity is calculated using eq. (21) [?]:

$$D_{\text{eff}} = \frac{e^2}{6\ \tau_l} \tag{21}$$

where e (m) is the thickness of the sample.

The result of the post-processing steps applied to the cycles of figure 3 is given in figure 4, which shows in detail that the first timelag is much longer than the following ones, which are all identical. In the following, the analysis is conducted on the final timelag; the particularities of the first cycle are discussed in subsection 5.2.

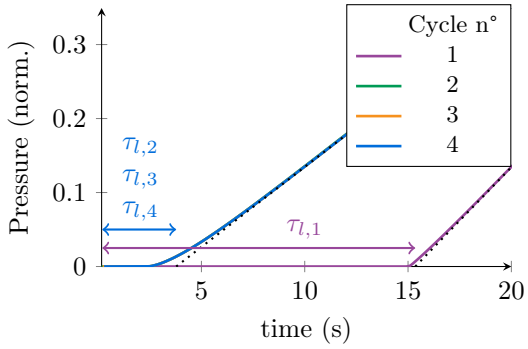

Figure 4: Output of the postprocessing steps applied to the permeation cycles presented in figure 3, simulated at 673 K. The pressure has been normalized so that maximum pressures are 1 at the end of the loading cycle (t=50 s). The first timelag (around 15 s) is notably longer than the following ones (around 3 s), which are all identical.

4.2. Influence of each trapping site on D_{eff} depending on the temperature range

The three-traps model obtained from the TDS simulations (see table 2) is used to replicate permeation experiments. The traps are added one by one in the simulations in order to pinpoint the contribution of each trapping site to the effective diffusivity. The results are shown in figure 5 and compared to experimental results, including the effective diffusivity taken from [?], which values are recalled in table 1.

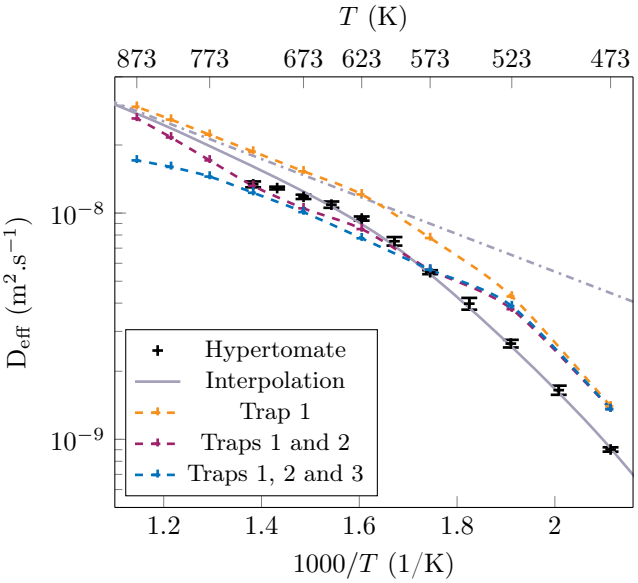

Figure 5: Comparison of MHIMS-simulated D_{eff}(T) and experimental D_{eff}(T). Traps are added one by one in order to show their influence. In particular, adding trap 2 seems to have an influence in the 523 K to 773 K range; trap 3 modifies effective diffusivity above 723 K. The dashdotted grey line represents interstitial diffusivity D introduced in equation 3.

Figure 5 shows that the model taking into account only the first trap gives a D_{eff}(T) law that resembles the interpolation, with an offset in the experimental temperature range, leading to an overestimation of effective diffusivity. The single-trap model agrees with the interstitial diffusivity above 623 K, which indicates that trap 1 has an influence in the 473 K-623 K region. Adding trap 2 makes D_{eff} drop below the experimental values in the 523 K to 773 K range. Both these models agree with the interpolation law at 873 K, which corresponds to interstitial diffusivity D at this temperature, i.e. the trapping sites have low enough energies for trapping not to interfere with permeation at 873 K and above. However, experimental points above 673 K show a different trend: the experimental increase of D_{eff} at higher temperatures is lower than the interpolation. Adding trap 3 caps this increase and gives a more satisfying plot at temperatures above 723 K.

This first comparison between the models, the experimental points and the interpolation shows that the capping witnessed on experimental points above 723 K can be explained by the presence of a high detrapping energy trap. Furthermore, traps seem to have an influence on specific temperature ranges, namely above 723 K for trap 3, between 523 K and 823 K for trap 2, and below 623 K for trap 1.

However, the final plot (corresponding to the three-traps model described in table 2) does not replicate the effective diffusivity experimental points satisfyingly: effective diffusivity is overestimated below 523 K, which is the range

where trap 1 drives D_{eff}. The addition of trap 2 makes effective diffusivity drop below the experimental values in the 523 K to 823 K range. This could be linked to the traps density: a higher density for a given trap could decrease effective diffusivity in the temperature range in which this given trap has an influence on permeation.

4.3. Model adjustment through traps densities correction

The density of each trap is adjusted manually in order to improve the comparison between the simulated and experimental effective diffusivities. The method followed is similar to that of subsection 4.2: traps are added one by one and their density is adjusted to improve the correspondence between effective diffusivities in the temperature range where this trap has an influence on permeation. The fit is considered satisfactory when the resulting effective diffusivity lies within the error bar of the experimental results. The results are presented in figure 6, and the initial and adjusted traps densities are given in table 3. The three-traps models with initial and adjusted densities are referred to as "initial model" and "adjusted model" in the following.

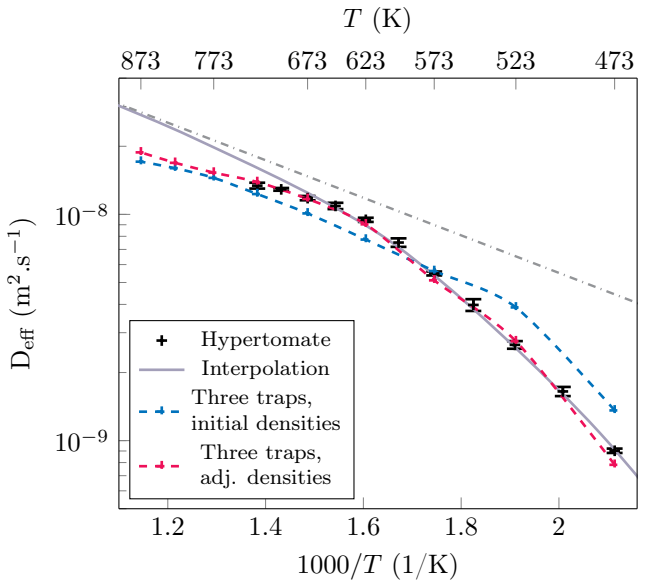

Figure 6: Comparison of experimental and simulated D_{eff}. Traps are added one by one in order to show the influence of each one of them. The dashdotted grey line represents interstitial diffusivity D introduced in equation 3.

Below 523 K, the initial model overestimates D_{eff}, which means that the density of the first trapping sites needs to be increased in order to get closer to experimental effective diffusivity. Between 573 K and 673 K, the initial model underestimates D_{eff}, which means that the density of trapping site 2 needs to be decreased to reproduce the experimental effective diffusivity. Above 673 K, the initial model yields effective diffusivity values that match the experimental ones: the density of the third trapping site does not need to be altered.

Detrapping energy (eV)	Initial density (m^{-3})	Adjusted density (m^{-3})	Ratio
0.51 eV	$6.01{\cdot}10^{25}$	$1.71{\cdot}10^{26}$	2.85
1.27 eV	$6.44{\cdot}10^{22}$	$2.11{\cdot}10^{22}$	0.33
1.65 eV	$3.88{\cdot}10^{23}$	$3.88{\cdot}10^{23}$	1

Table 3: Former and corrected densities of each trap after the effective diffusivity fit. The density of the third trap remains the same.

Table 3 indicates that the density of trapping site 1 has been increased by a factor of 2.85. This density is higher than the values of N_t evaluated by other authors through permeation, which are recalled in table 1. This higher density value could be explained by the fact that the Eurofer97 samples used in Hypertomate and TEDDI did not undergo any annealing or thermal treatment prior to the experiments, which can lead to a higher density of defects.

4.4. Effective solubility

Hydrogen permeability in Eurofer97 can also be obtained from the permeation simulations using

$$J = \frac{\Phi}{e} P_{\text{loading}}^{1/2} \tag{22}$$

where J (mol.s^{-1}) is the permeation flux in steady-state, Φ is the permeability ($\text{mol.m}^{-1}.\text{Pa}^{-1/2}.\text{s}^{-1}$), e is the thickness of the sample (m) and P_{loading} is the loading pressure (Pa). Equation (22) only applies if the permeation regime is diffusion-limited. Using permeability, hydrogen effective solubility K_{eff} ($\text{mol.m}^{-3}.\text{Pa}^{-1/2}$) can be evaluated as

$$K_{\text{eff}} = \frac{\Phi}{D_{\text{eff}}} \tag{23}$$

$$= K \cdot \left(1 + \frac{N_{\text{t}}}{N_{\text{L}}} \exp\left(\frac{E_b}{k_B T}\right)\right) \tag{24}$$

in which appears the interstitial solubility K:

$$K(T) = K_0 \cdot \exp\left(-\frac{E_K}{k_B T}\right) \tag{25}$$

In (25), K_0 ($\text{mol.m}^{-3}.\text{Pa}^{-1/2}$) is the pre-exponential solubility factor and E_K (eV) the solution energy of hydrogen in interstitial sites.

The effective solubility as obtained with permeation experiments and MHIMS simulations is shown in figure 7.

In the temperature range corresponding to the experiments, the predicted effective solubility is satisfactory. At lower temperatures, the effective solubility given in table 1, Hypertomate results and the

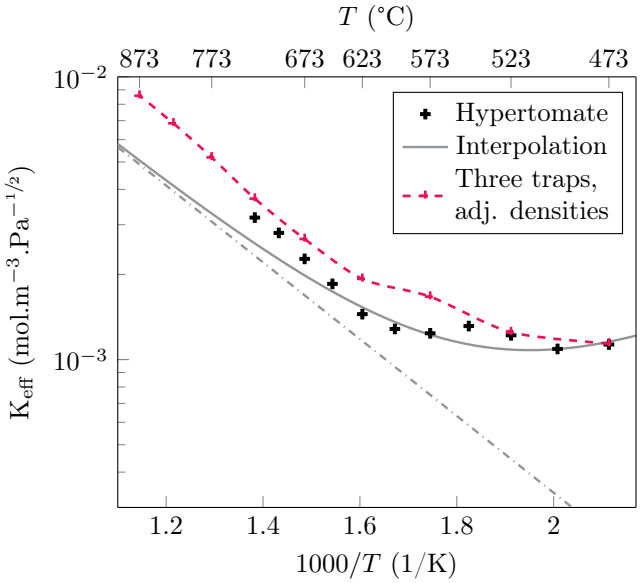

Figure 7: Hydrogen effective solubility in Eurofer97, obtained experimentally and with MHIMS simulations. The dashdotted grey line represents interstitial solubility K introduced in equation (25).

three-traps model are in agreement. At temperatures above 673 K, experimental measurements of effective diffusivity are closer to the values predicted by MHIMS than to the interpolation corresponding to Oriani's model. This trend seems to accentuate at temperatures above 723 K. The influence of this point on inventory evaluation is discussed in subsection 5.3.

5. Impact of traps reversibility on permeation results

In section 4, the three-traps adjusted model of hydrogen interactions in Eurofer97 was validated. In this part, the reversibility of trapping sites is used to investigate their effect on the physical quantities that are accessible with a permeation experiment, such as the timelag. In a final subsection, timelag and inventory evaluations obtained using the effective transport parameters (effective diffusivity and effective solubility) are compared to evaluations relying on the detailed three-traps model.

5.1. Trapping sites reversibility

Subsections 4.2 and 4.3 have shown that each trapping site has an effect on the effective diffusivity in a limited temperature range. This has been shown to be caused by the reversibility of the trapping sites [**?** **?** **?** **?** **?** **?**]. Usually, trapping sites with a low detrapping energy are considered reversible, as they allow hydrogen to easily detrap. Most of the experiments from which this definition stems are linked to structural studies, especially hydrogen embrittlement [**?** **?** **?** **?**], conducted at room temperature. In the case of fusion applications, the temperature of permeation-relevant material during their lifetime can range from low temperatures (during maintenance operations), medium temperatures (pipe forest between 553 K and 773 K [**?**]) to higher ones (up to 783 K for the HCPB scenario of the DEMO first wall [**?**]). Therefore, the reversibility considered in this work takes into account the temperature range and the time frame of the permeation cycles.

In the permeation simulations, during the loading phase, the sites (mobile, trap i) retain hydrogen atoms, which are released during the resting phase. For a given temperature, the rate at which this release occurs is highly dependent on the type of site and on the corresponding detrapping energy. Schematically, the higher the detrapping energy is, the longer it will take for the trapping site to release hydrogen atoms. In the case of a high detrapping energy site, this detrapping rate is low enough to be neglected if the considered horizon is short term (a few minutes, in the case of permeation experiments) or mid-term (months in the case of reactor walls): the trapping site is deemed irreversible.

Figure 8 gives an illustration of reversibility in Eurofer97 at 573 K with adjusted densities during the course of two permeation cycles consisting each of 1000 s of loading and 1000 s of resting. At this temperature, interstitial sites and trap 1 are fully reversible, because they release their total inventory during the resting phase. However, trap 2 is only partially reversible and trap 3 is not reversible, as particles are not released during the resting phase. Based on these observations, we can infer that the reversibility of interstitial sites, traps 1 and 2 have an impact on the kinetics of permeation at this temperature, and that trap 3 does not have an impact at this temperature, except for the first cycle (see section 5.2). This indicates that trap 3 is irreversible for this given temperature.

In order to quantify this, reversibility of site i is formalized as $\Delta \mathrm{I}_i$, which is the difference between the maximum inventory reached during loading and the inventory at the end of resting, as shown in figure 8. This quantity is evaluated for each site (mobile and traps) during permeation cycles simulated with temperatures ranging from 473 K to 873 K. The contribution of site i to the total inventory variation during a permeation cycle is given by

$$\%\Delta \mathrm{I}_i = \frac{\Delta \mathrm{I}_i}{\sum_i \Delta \mathrm{I}_i} \tag{26}$$

The results of this contribution analysis are shown in figure 9, giving a detailed understanding of reversibility in the operational temperature range of Eurofer97. The contribution of the upstream and downstream surfaces has not been taken into account to simplify the analysis, as the associated desorption kinetics are almost instantaneous and therefore have a negligible effect on the dynamics of permeation.

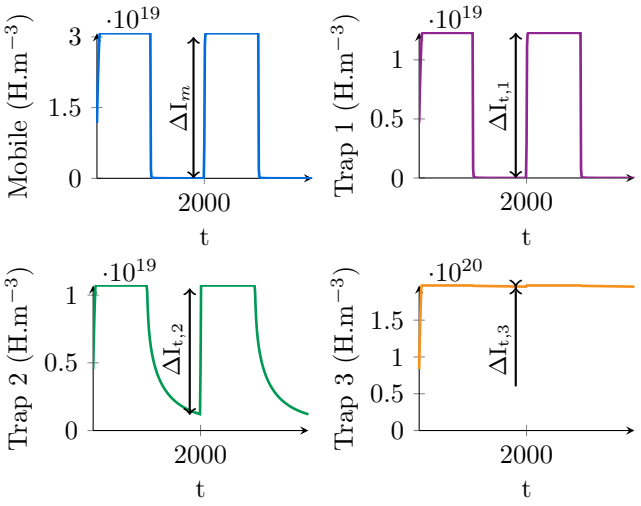

Figure 8: Evolution of the mobile and trapped inventory during two permeation cycles (1000 s loading, 1000 s resting) in Eurofer97 at 573 K. Interstitial sites and trap 1 are fully reversible, i.e. they release all the particles that were trapped while loading during the resting phase. Trap 2 is partially reversible at this temperature and for the resting duration considered. Trap 3 is not reversible: particles are not released during the resting phase.

Below 523 K, permeation is dominated by the first trap. In the mid-range (523 K to 700 K), interstitial sites become dominant and the contribution of trap 2 increases, reaching a maximum around 623 K. Looking back at figure 5, this temperature corresponds to the inflection of the curve caused by the addition of trap 2 to the model. Above 700 K, the contribution of trap 3 increases up to 42 %, which shows that this trapping site influences permeation during its transient phase in the high-temperature range. This effect is linked to the drop in effective diffusivity noticed in subsection 4.3: above 700 K, the addition of the third trap to the model influences permeation enough to make effective diffusivity diverge from the interpolation law obtained through equation (20).

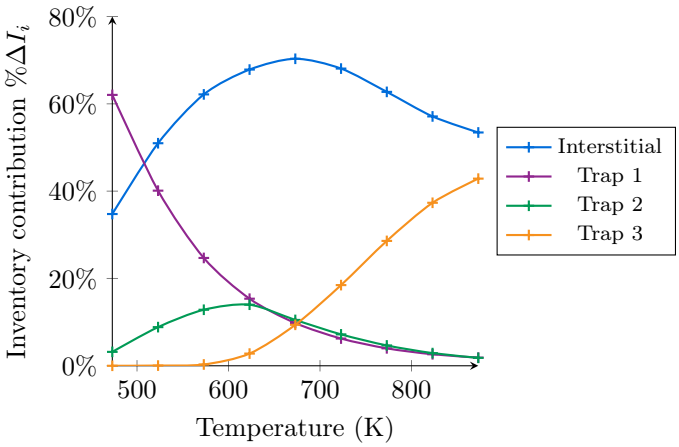

Figure 9: Reversibility of the traps and interstitial sites, expressed in percentage of the total permeation flux

In [?], Pressouyre separates the trapping sites present in Fe-Ti into reversible or irreversible trapping sites, using the interval between the energies of these sites for the reversible to irreversible transition. This analysis is performed at room temperature. Following the same method and using figure 9, we can determine that trapping site 1 is reversible at 473 K while trapping sites 2 and 3 are irreversible: the transition from reversible to irreversible takes place in the interval between the detrapping energies of these sites. This gives us a criterion for this transition, that can be extended to higher temperatures using the E_b/k_bT quantity as shown in figure 10, which confirms the results presented in 9 in terms of reversibility or irreversibility depending on the temperature.

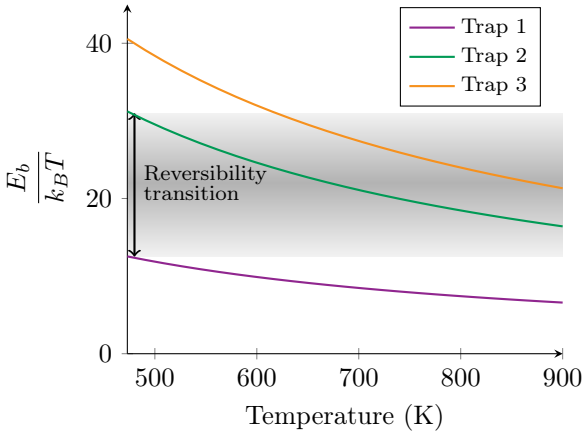

Figure 10: Evolution of the E_b/k_BT ratio versus temperature, shown for each Eurofer trapping site. The reversibility transition, based on low temperature reversibility, is extended to higher temperatures.

5.2. Analysis of the first timelag

As observed in figures 3 and 4, the first timelag obtained through simulations may be much longer than the next timelags when the simulation includes several permeation cycles and at least one irreversible trapping site. This effect has been witnessed experimentally in steels and iron [? ? ? ?]. An example of this effect in Eurofer97 at 523 K is shown in figure 11, where the breakdown of the detailed inventory shows that the extra time corresponds to the filling of the irreversible trap.

During the first loading phase, saturation of traps 2 and 3 takes place first, followed closely by saturation of trap 1. The corresponding timelag is 129 s. Given their detrapping energies (1.27 eV and 1.65 eV) and the relatively low temperature of the run (523 K), trap 3 remains saturated until the end of the simulation and trap 2 desorbs at a slow rate (because trap 2 is not fully reversible at 523 K, as indicated by figures 9 and 10). In particular, we can notice that traps 1 and 2 are filled at a much quicker rate during the second loading phase, resulting in a shorter timelag (16 s). This effect can be expected to be particularly prominent in the low-temperature range or in the presence of trapping sites with a high detrapping

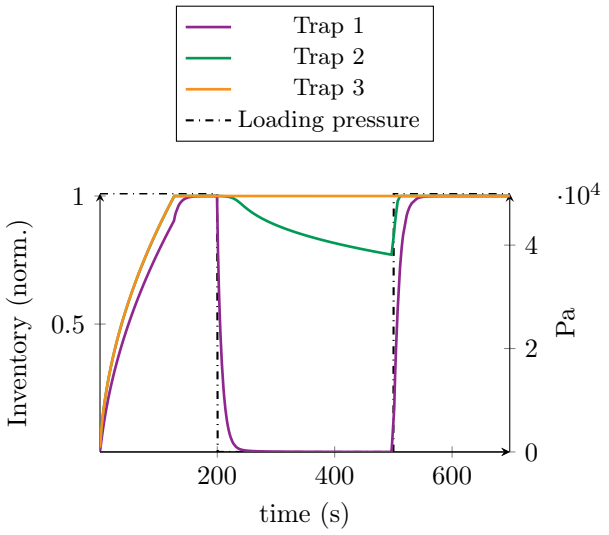

Figure 11: Breakdown of the (normalized) trapping inventories during two loading phases and a resting phase at 523 K. Trap 3 remains saturated after $t = 120$ s and no longer impacts permeation after this time mark, which explains that the second timelag is shorter than the initial one.

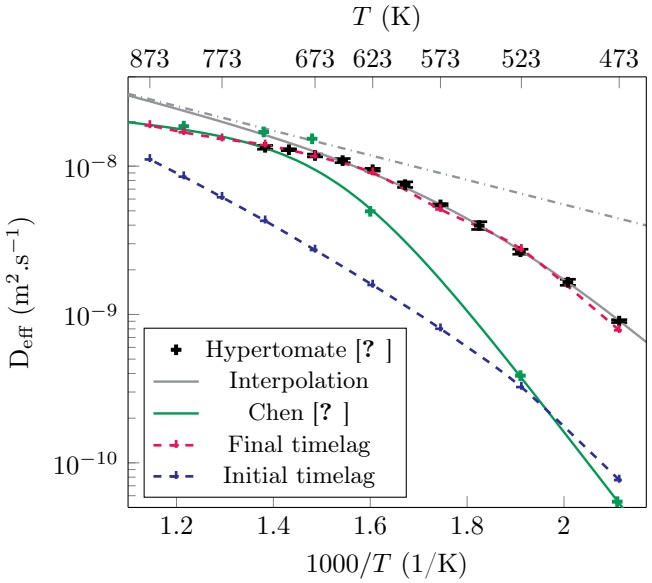

Figure 12: Comparison of the initial vs. steady-state timelag on effective diffusivity, using the adjusted densities model. The interpolation law and experimental points given in [?], corrected in order to be compared with hydrogen results are shown. The dashdotted line represents interstitial diffusivity D introduced in equation (3).

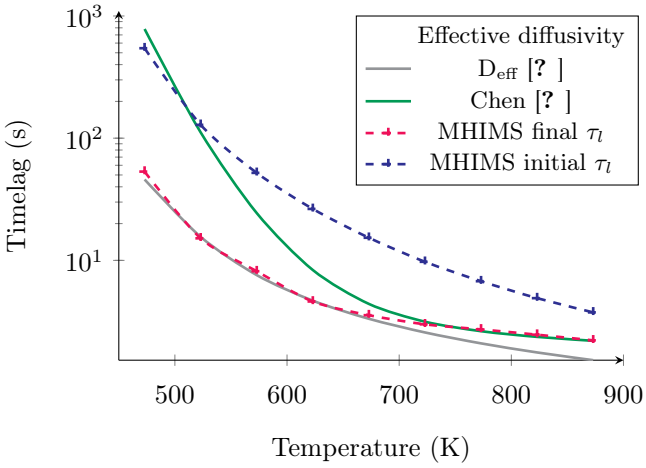

Figure 13: Comparison of the timelags evaluated using equation (21) with several effective diffusivities, assuming a sample thickness of 500 µm. At higher temperatures, the effect of the irreversible trap vanishes and all plots show a similar trend; however, at lower temperatures, the first timelag and the timelag evaluated using [?] are up to an order of magnitude higher than other timelags.

energy. In order to study it, four consecutive permeation cycles were simulated with temperatures ranging from 423 K to 873 K. With this method, the timelag obtained with the first cycle ("initial timelag") differs from the next three, which are all identical and will be referred to as "final timelag" in the following.

Figure 12 shows the effective diffusivity corresponding to the first cycle as compared to the one corresponding to the following cycles. Although the shapes are similar, the time needed for the permeation flux to reach steady-state is much longer in the case of the first cycle, which results in a discrepancy between effective diffusivities that worsens at lower temperatures.

The effective diffusivity interpolation given in [?] (shown in the figure) reports effective diffusivity values that are significantly lower than previously reported ones in the lower temperature range [? ? ?]. This discrepancy could be explained by the initial timelag bias. In the low temperatures range, the data given in [?] matches the initial timelag results, but follows the final timelag at higher temperatures and even includes the effective diffusivity drop that was shown to be caused by the third trap in subsection 4.2. A possible explanation for the discrepancy between experimental diffusivities could be that the diffusion reported in [?] corresponds to an initial timelag. As soon as the number of permeation cycles performed on a given sample increases, this bias vanishes and the reported D_{eff} values get closer to previously reported ones.

Using equation (21) and assuming a sample thickness of 500 µm, the effective diffusivities shown in figure 12 can be translated into timelags. The comparison between these timelags is given in figure 13. At higher temperatures, the high-energy trap is reversible: the plots show a common trend, although the first timelag remains higher than the other ones. At lower temperatures, the high-energy trap is irreversible and the first timelag is more than ten times longer than other timelags, except for Chen's [?]. In particular, figure 13 can be used to illustrate that equation (21) can only be used to evaluate the timelag if the irreversible traps (at a given temperature) are already filled with hydrogen isotopes. Outside of this range, the

resulting timelag is underestimated.

5.3. *Comparison with inventory simulations performed at system level*

System-level simulations of permeation and retention are necessary for the design of several parts of fusion power plants, among which breeding blankets [**?**]. In order to take into complex interactions (magneto-hydrodynamic effects [**?**], interfaces between distinct elements [**?**]), these simulations require simplified modeling of the permeation and retention dynamics. Most of these codes evaluate the tritium permeation through the breeding blankets based on interstitial diffusivity as presented in equation (3) [**? ?**]. The choice of D instead of D_{eff} implies that the trapping behavior is neglected in these evaluations. One of the consequences of this simplification is the underestimation of the breakthrough time, as trapping increases the timelag (see figure 13). In some cases, solubility is introduced through the use of the Sieverts' boundary condition [**? ?**]:

$$C = K_x \cdot \sqrt{P_{\text{loading}}} \tag{27}$$

where K_x is either K_{eff}, which takes into account the trapping effects, or K that gives the mobile concentration in the sample. Such a model does not discriminate between mobile and trapped particles: the concentration considered here is C and pertains to both. Here again, the use of interstitial solubility instead of effective diffusivity K_{eff} shows that trapping is not taken into account.

In order to bridge the gap between simplified system-level codes and detailed diffusion-trapping codes such as MHIMS, intermediary simulations can be performed as presented in [**?**] which uses the open source framework OpenFOAM to evaluate the permeation fluxes through a breeding unit. This "component level" simulation uses the effective transport parameters D_{eff} and K_{eff} to account for the trapping effects.

Using interstitial or effective transport parameters instead of a detailed McNabb & Foster model has an influence on the evaluation of retention. The difference between these approaches can be illustrated simply by comparing the inventory as evaluated using two methods:

- With a MHIMS simulation of Eurofer97 slab with thickness $e = 500$ µm, taking into account the three-traps model with adjusted densities of section 4.3 and Sieverts law as the boundary condition with $P_{\text{loading}} = 5 \cdot 10^4$ Pa;
- Assuming an equilibrium concentration profile and using the value given by equation (27), the inventory is simply $I = C \cdot e = K_x \cdot \sqrt{P_{\text{loading}}} \cdot e$. This evaluation is performed with K (interstitial solubility) and with K_{eff} (effective solubility).

The result of this comparison is given in figure 14; the output of the MHIMS simulation is given in terms of mobile and total retention.

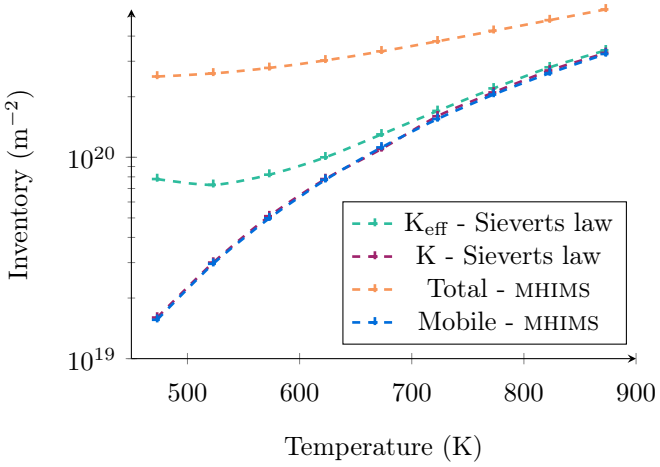

Figure 14: Comparison of the inventories as evaluated with MHIMS and using Sieverts' law associated with K or K_{eff}. Mobile evaluation relying on Sieverts' law and MHIMS are in agreement, whereas total inventory is underestimated with Sieverts' law as compared to MHIMS.

Figure 14 shows that the evaluation of mobile particles inventory relying on Sieverts' law and given by MHIMS are in agreement. Regarding the total inventory, the effective solubility evaluation implies an underestimation by a factor 3 at 473 K and by a factor 1.5 at 873 K. The information given by effective solubility only regards trapping sites which reversibility has an influence on the permeation dynamics. At lower temperatures (below 550 K), the underestimation accentuates because trap 3 is irreversible. This observation shows that the use of solubility and/or effective solubility in system level simplified models does not yield a satisfactory prediction of the total inventory, as it overlooks reversibility effects highlighted in this work.

6. Conclusion

Permeation and TDS experiments are simulated using MHIMS to extract a model of the hydrogen-Eurofer97 interactions, including diffusion and trapping. Three trapping sites with detrapping energies of 0.51 eV, 1.27 eV and 1.65 eV are necessary to describe trapping in this material. Using simulations of permeation cycles, the influence of each trapping site on the permeation of hydrogen is investigated: the 0.51 eV trapping site impacts permeation below 523 K, the 1.27 eV trapping site impacts permeation from 573 K to 673 K and the high-energy trapping site at 1.65 eV has an influence at temperatures above 673 K.

The influence of a given trapping site on permeation is linked to its reversibility, which states whether a trapping site containing hydrogen is likely to release its content [**? ? ? ? ? ?**]. Reversibility as a notion can be used independently of temperature (e.g. in the field of

hydrogen embrittlement, with steels operating at room temperature) or be extended in order to take into account the temperature operating range of the material (as mentioned by Shu et al. [**?**] for Fe-Ti alloys), which is especially needed for fusion materials. In order to take this temperature dependence into account, the present work evaluates the inventory of each of the three Eurofer97 trapping sites to quantify their reversibility. Using this method, the 0.51 eV trapping site is shown to be reversible at low temperatures, while the 1.27 eV trapping site is reversible above 573 K. The 1.65 eV trapping site is only reversible at temperatures above 673 K.

In the final section, the reversibility of trapping sites is used to explain the discrepancy between estimations of tritium inventory and timelag evaluated with a full diffusion-trapping model such as MHIMS or using effective transport parameters, in the case of system-level codes.

This work suggests that careful simulations of permeation cycles coupled with TDS analysis yield a cohesive model describing the interaction of hydrogen with Eurofer97, which is a critical point for the evaluation of inventory and permeation at a system level [**?**]. The assumptions that are required to validate the effective diffusivity model are not compatible with the irreversibility of the trapping sites in Eurofer97. Therefore, the estimation of tritium inventory and permeation at system level requires a model that takes into account all trapping sites, using the McNabb & Foster equations such as FESTIM [**?**] or a generalized Oriani approximation as developed in [**?**].

Although the analysis presented in this work has been conducted on Eurofer97, the method used could be applied to any permeation-relevant fusion material and even extended in order to take into account neutron exposure, which will result in the dynamic creation of potentially irreversible trapping sites.

Acknowledgements

This work has been carried out within the framework of the EUROfusion Consortium and has received funding from the Euratom research and training programme 2014-2018 and 2019-2020 under grant agreement no. 633053. The views and opinions expressed herein do not necessarily reflect those of the European Commission.

References

[1] T. Tanabe, Tritium issues to be solved for establishment of a fusion reactor, Fusion Engineering and Design 87 (5) (2012) 722–727, tenth International Symposium on Fusion Nuclear Technology (ISFNT-10).

[2] G. De Temmerman, M. Baldwin, D. Anthoine, K. Heinola, A. Jan, I. Jepu, J. Likonen, C. Lungu, C. Porosnicu, R. Pitts, Efficiency of thermal outgassing for tritium retention measurement and removal in ITER, Nuclear Materials and Energy 12 (2017) 267–272, proceedings of the 22nd International Conference on Plasma Surface Interactions 2016, 22nd PSI.

[3] E. Hodille, R. Delaporte-Mathurin, J. Denis, M. Pecovnik, E. Bernard, Y. Ferro, R. Sakamoto, Y. Charles, J. Mougenot, A. D. Backer, C. Becquart, S. Markelj, C. Grisolia, Modelling of hydrogen isotopes trapping, diffusion and permeation in divertor monoblocks under ITER-like conditions, Nuclear Fusion 61 (12) (2021) 126003.

[4] R. Arredondo, K. Schmid, F. Subba, G. Spagnuolo, Preliminary estimates of tritium permeation and retention in the first wall of DEMO due to ion bombardment, Nuclear Materials and Energy 28 (2021) 101039.

[5] M. Shimada, C. Taylor, Improved tritium retention modeling with reaction-diffusion code TMAP and bulk depth profiling capability, Nuclear Materials and Energy 19 (2019) 273–278.

[6] E. A. Hodille, E. Bernard, S. Markelj, J. Mougenot, C. S. Becquart, R. Bisson, C. Grisolia, Estimation of the tritium retention in ITER tungsten divertor target using macroscopic rate equations simulations, Physica Scripta T170 (2017) 014033.

[7] A. Kohyama, A. Hishinuma, D. S. Gelles, R. L. Klueh, W. Dietz, K. Ehrlich, Low-activation ferritic and martensitic steels for fusion application, Journal of Nuclear Materials 233-237 (1996) 138–147.

[8] G. Federici, L. Boccaccini, F. Cismondi, M. Gasparotto, Y. Poitevin, I. Ricapito, An overview of the EU breeding blanket design strategy as an integral part of the DEMO design effort, Fusion Engineering and Design 141 (2019) 30–42.

[9] F. Montupet-Leblond, L. Corso, M. Payet, R. Delaporte-Mathurin, E. Bernard, Y. Charles, J. Mougenot, S. Vartanian, E. Hodille, C. Grisolia, Permeation and trapping of hydrogen in Eurofer97, Nuclear Materials and Energy 29 (2021) 101062.

[10] G. Esteban, A. Peña, I. Urra, F. Legarda, B. Riccardi, Hydrogen transport and trapping in Eurofer97, Journal of Nuclear Materials 367-370 (2007) 473–477.

[11] A. Aiello, I. Ricapito, G. Benamati, R. Valentini, Hydrogen isotopes permeability in Eurofer97 martensitic steel, Fusion Science and Technology 41 (2002) 872–876.

[12] Y. Martynova, M. Freisinger, A. Kreter, B. Göths, S. Möller, A. Terra, D. Matveev, M. Rasiński, B. Unterberg, S. Brezinsek, C. Linsmeier, Impact of Kr and Ar seeding on D retention in ferritic-martensitic steels after high-fluence plasma exposure, Nuclear Materials and Energy 17 (2018) 307–313.

[13] E. Legrand, X. Feaugas, J. Bouhattate, Generalized model of desorption kinetics: Characterization of hydrogen trapping in a homogeneous membrane, International Journal of Hydrogen Energy 39 (16) (2014) 8374–8384.

[14] L. Cheng, L. Li, X. Zhang, J. Liu, K. Wu, Numerical simulation of hydrogen permeation in steels, Electrochimica Acta 270 (2018) 77–86.

[15] T. Schaffner, A. Hartmaier, V. Kokotin, M. Pohl, Analysis of hydrogen diffusion and trapping in ultra-high strength steel grades, Journal of Alloys and Compounds 746 (2018) 557–566.

[16] B. Yang, L. Li, L. Cheng, Numerical evaluation on analysis methods of trapping site density in steels based on hydrogen permeation curve, Materials 13 (17) (2020).

[17] A. Oudriss, J. Creus, J. Bouhattate, E. Conforto, C. Berziou, C. Savall, X. Feaugas, Grain size and grain-boundary effects on diffusion and trapping of hydrogen in pure nickel, Acta Materialia 60 (19) (2012) 6814–6828.

[18] A. Díaz, A. Zafra, E. Martínez-Pañeda, J. Alegre, J. Belzunce, I. Cuesta, Simulation of hydrogen permeation through pure iron for trapping and surface phenomena characterisation, Theoretical and Applied Fracture Mechanics 110 (2020) 102818.

[19] G. Pressouyre, I. Bernstein, A quantitative analysis of hydrogen trapping, Metallurgical transactions A 9 (11) (1978) 1571–1580.

[20] S. J. Zinkle, Advanced materials for fusion technology, Fusion Engineering and Design 74 (1) (2005) 31–40, proceedings of the 23rd Symposium of Fusion Technology.

[21] A. Drexler, W. Siegl, W. Ecker, M. Tkadletz, G. Klösch,

H. Schnideritsch, G. Mori, J. Svoboda, F. Fischer, Cycled hydrogen permeation through Armco iron – a joint experimental and modeling approach, Corrosion Science 176 (2020) 109017.
[22] A. McNabb, P. K. Foster, A new analysis of the diffusion of hydrogen in iron and ferritic steels, Transactions of the Metallurgical Society of AIME 27 (1963) 227–618.
[23] E. A. Hodille, X. Bonnin, R. Bisson, T. Angot, C. S. Becquard, J. M. Layet, C. Grisolia, Macroscopic rate equation modeling of trapping/detrapping of hydrogen isotopes in tungsten materials, Journal of Nuclear Materials 467 (2015) 424–431.
[24] A. H. Krom, A. Bakker, Hydrogen trapping models in steel, Metallurgical and materials transactions B 31 (6) (2000) 1475–1482.
[25] I. Moro, Fragilisation par l'hydrogène gazeux d'un acier ferrito-perlitique de grade API X80, Ph.D. thesis (2009).
[26] R. Oriani, The diffusion and trapping of hydrogen in steel, Acta Metallurgica 18 (1970) 147–157.
[27] Z. Chen, X. Hu, M. Ye, B. D. Wirth, Deuterium transport and retention properties of representative fusion blanket structural materials, Journal of Nuclear Materials 549 (2021) 152904.
[28] E. A. Hodille, L. Begrambekov, J. Pascal, O. Saidi, J. M. Layet, B. Pégourié, C. Grisolia, Hydrogen trapping in carbon film: From laboratories studies to tokamak applications, International Journal of Hydrogen Energy 39 (2014) 20054–20061.
[29] E. Hodille, A. Založnik, S. Markelj, T. Schwarz-Selinger, C. Becquart, R. Bisson, C. Grisolia, Simulations of atomic deuterium exposure in self-damaged tungsten, Nuclear Fusion 57 (5) (2017) 056002.
[30] V. Oliveira, K. Zilnyk, H. Sandim, Thermodynamic simulation of reduced activation ferritic-martensitic Eurofer97 steel, Journal of Phase Equilibria and Diffusion 38 (2017) 208–216.
[31] G. A. Esteban, L. A. Sedano, B. Mancinelli, K. Douglas, Diffusion and surface-limited transport parameters of deuterium in Incoloy 800, Tech. rep., I-21020 Ispra - Italy (2001).
[32] J. Lee, C. Park, H. Park, N. Kang, Effective hydrogen diffusion coefficient for CoCrFeMnNi high-entropy alloy and microstructural behaviors after hydrogen permeation, International Journal of Hydrogen Energy 45 (16) (2020) 10227–10232.
[33] L. Giancarli, M. Abdou, D. Campbell, V. Chuyanov, M. Ahn, M. Enoeda, C. Pan, Y. Poitevin, E. Rajendra Kumar, I. Ricapito, Y. Strebkov, S. Suzuki, P. Wong, M. Zmitko, Overview of the ITER TBM program, Fusion Engineering and Design 87 (5) (2012) 395–402, tenth International Symposium on Fusion Nuclear Technology (ISFNT-10).
[34] L. Boccaccini, G. Aiello, J. Aubert, C. Bachmann, T. Barrett, A. Del Nevo, D. Demange, L. Forest, F. Hernandez, P. Norajitra, G. Porempovic, D. Rapisarda, P. Sardain, M. Utili, L. Vala, Objectives and status of EUROfusion DEMO blanket studies, Fusion Engineering and Design 109-111 (2016) 1199–1206, proceedings of the 12th International Symposium on Fusion Nuclear Technology-12 (ISFNT-12).
[35] T. Gilardi, C. Moreno, C. Grisolia, Comparison of two modelling tools for the evaluation of tritium and hydrogen transfers in nuclear reactors or complex systems, Fusion Engineering and Design 166 (2021) 112278.